

Statistical analysis of binary stars from the Gaia catalogue DR2

PETR ZAVADA^{1,1} AND KAREL PÍŠKA^{1,1}

¹*Institute of Physics of the Czech Academy of Sciences, Na Slovance 2, 182 21 Prague 8, Czech Republic*

(Accepted by the Astronomical Journal: November 15, 2019)

ABSTRACT

We have developed a general statistical procedure for analysis of 2D and 3D finite patterns, which is applied to the data from recently released Gaia-ESA catalogue DR2. The 2D analysis clearly confirms our former results on the presence of binaries in the former DR1 catalogue. Our main objective is the statistical 3D analysis of DR2. For this, it is essential that the DR2 catalogue includes parallaxes and data on the proper motion. The analysis allows us to determine for each pair of stars the probability that it is the binary star. This probability is represented by the function $\beta(\Delta)$ depending on the separation. Further, a combined analysis of the separation with proper motion provides a clear picture of binaries with two components of the motion: parallel and orbital. The result of this analysis is an estimate of the average orbital period and mass of the binary system. The catalogue we have created involves 80560 binary candidates.

1. INTRODUCTION

In this paper we analyze the recent data from the new catalogue DR2 [Gaia Collaboration \(2018\)](#) obtained by the Gaia-ESA mission. If compared with the previous DR1 catalogue [Gaia Collaboration \(2016b,a\)](#), the DR2 contains the cleaner data complemented with parallaxes and data on the 2D proper motion. Parallaxes allow us to determine the distance of the stars, so we can substantially enlarge our former DR1 analysis [Zavada&Píška \(2018\)](#) and work with the 3D patterns of moving stars.

In the present study, we focus on the statistical analysis of the presence of binaries. This topic is related to the recent studies of various aspects of binaries with the use of the catalogues DR1 ([Oelkers \(2017\)](#); [Oh \(2017\)](#)) and DR2 ([Ziegler \(2018\)](#); [Jiménez-Esteban et al. \(2019\)](#)). These authors, apart from their own results, present an up-to-date overview of important findings on binary stars. Other important papers exploring wide binaries can be cited from the era before Gaia, for example [Cabalero \(2009\)](#); [Close et al. \(1990\)](#). However, our approach and objectives are rather different, so the results obtained are complementary.

Methodology for 2D analysis has been described in detail in our above-quoted paper. In Sec.2 we repeat its essence and perform generalization for the 3D case. For 2D analysis in Sec.3 we take the same region in DR2 catalogue as we used in the DR1, so we can compare results from both corresponding data sets.

Principal results are obtained from the 3D analysis of a sample of DR2 data and are presented in Sec.4. This part deals with two issues: the analysis of 3D separations and the analysis of proper motion of pairs of sources. The combination of both insights provides essential information about the statistical set of binaries. Obtained results are discussed in Sec.5. Here we define the probabilistic function $\beta(\Delta)$, which is important for discussion on the occurrence of binaries. Our present catalogue of binary candidates is described in Sec.6, where we also shortly discuss its content and overlap with the catalogue JEC - [Jiménez-Esteban et al. \(2019\)](#).

The brief summary of the paper is presented in Sec.7. The appendix is devoted to the derivation of some relations important for our statistical approach. The most important are distributions of separations of random sources uniformly distributed inside circles or spheres of unit diameter. Significant role of these functions for our approach is explained in Sec.2.

2. METHODOLOGY

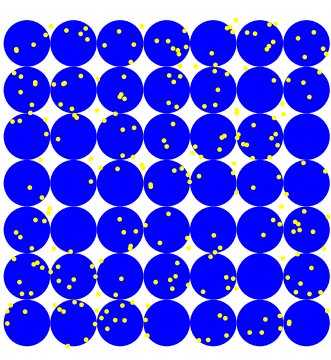


Figure 1. Grids of 2D (*left*) and 3D (*right*) events with uniform distributions of the stars.

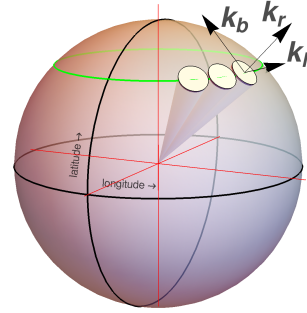
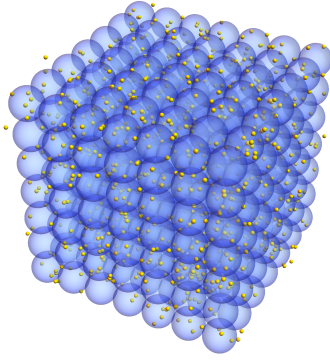


Figure 2. Galactic reference frame defined by galactic longitude and latitude with an event local frame defined by orthonormal basis $\mathbf{k}_r, \mathbf{k}_l, \mathbf{k}_b$.

The methods are designed for analysis of the distribution of stars inside circles or spheres covering the chosen region of the sky, as sketched in Fig.1. These 2D and 3D patterns of stars we call events. Input data for the generation of the event grids are supposed in the galactic reference frame. So, the position \mathbf{L} of a source is defined by spherical coordinates L, l and b (distance from the sun, galactic longitude and latitude):

$$\mathbf{L} = L\mathbf{n}; \quad \mathbf{n} = (\cos b \cos l, \cos b \sin l, \sin b), \quad (1)$$

$$-\frac{\pi}{2} \leq b \leq \frac{\pi}{2}, \quad -\pi < l \leq \pi.$$

In the centre of circles or spheres we define local orthonormal frame defined by the basis:

$$\begin{aligned} \mathbf{k}_r &= \mathbf{n}_0 = (\cos b_0 \cos l_0, \cos b_0 \sin l_0, \sin b_0), \\ \mathbf{k}_l &= (-\sin l_0, \cos l_0, 0), \\ \mathbf{k}_b &= (-\sin b_0 \cos l_0, -\sin b_0 \sin l_0, \cos b_0), \end{aligned} \quad (2)$$

where $\mathbf{k}_r = \mathbf{n}_0(b_0, l_0)$ defines angular position of the event centre. Unit vector \mathbf{k}_l is perpendicular to \mathbf{k}_r and has direction of increasing l , see Fig.2. Unit vector \mathbf{k}_b is defined as $\mathbf{k}_b = \mathbf{k}_r \times \mathbf{k}_l$ and has direction of increasing b . Vector \mathbf{k}_r has radial direction, perpendicular vectors \mathbf{k}_b and \mathbf{k}_l lies in the transverse plain.

2.1. Definition of events

The 2D event of the multiplicity M is a set of stars with angular positions \mathbf{n}_i inside a circle with the event centre \mathbf{n}_0 and a small angular radius ρ_2 :

$$|\mathbf{n}_i - \mathbf{n}_0| \leq \rho_2, \quad i = 1, \dots, M. \quad (3)$$

With the use of event local basis (2), the local coordinates are defined as

$$x_i = \mathbf{n}'_i \cdot \mathbf{k}_l, \quad y_i = \mathbf{n}'_i \cdot \mathbf{k}_b; \quad \mathbf{n}'_i = \mathbf{n}_i - \mathbf{n}_0. \quad (4)$$

We define 2D event as the set:

$$\{x_i, y_i\}; \quad x_i^2 + y_i^2 \leq \rho_2^2, \quad i = 1, \dots, M. \quad (5)$$

Since the DR2 catalogue involves also data on parallaxes, we can similarly generate also the 3D events - patterns of the M sources with position \mathbf{L}_i inside the spheres with the centre \mathbf{L}_0 and radius ρ_3 :

$$|\mathbf{L}_i - \mathbf{L}_0| \leq \rho_3, \quad i = 1, \dots, M. \quad (6)$$

With the use of the star positions (1) and local basis (2) we define local coordinates $\{X_i, Y_i, Z_i\}$ as

$$X_i = \mathbf{N}_i \cdot \mathbf{k}_l, \quad Y_i = \mathbf{N}_i \cdot \mathbf{k}_b, \quad Z_i = \mathbf{N}_i \cdot \mathbf{k}_r; \quad (7)$$

$$\mathbf{N}_i = L_i \mathbf{n}_i - \mathbf{L}_0, \quad L_i[\text{pc}] = \frac{1000}{p_i[\text{mas}]}, \quad (8)$$

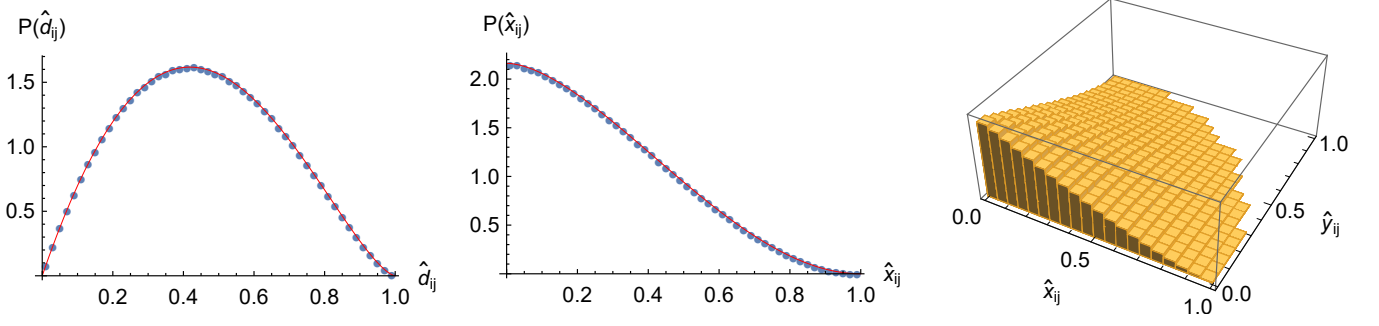


Figure 3. MC distributions of separations of uniformly generated stars (points). The red curves represent the functions (12) and (13). The Monte-Carlo statistics corresponds to 5×10^5 events of multiplicity $M = 5$.

where p_i is parallax, L_i is distance of the star. 3D event is defined as the set:

$$\{X_i, Y_i, Z_i\}; \quad X_i^2 + Y_i^2 + Z_i^2 \leq \rho_3^2, \quad i = 1, \dots, M. \quad (9)$$

2.2. 2D methods

The first method is based on the Fourier analysis of 2D events, where we have introduced characteristic functions $\Theta_n(M)$ depending on the event multiplicity M . These functions are generated by a set of events and measure statistical deviations from uniform distribution of stars ($\Theta_n(M) = 1$), for instance a tendency to clustering ($\Theta_n(M) > 1$) or anti-clustering ($0 < \Theta_n(M) < 1$). Details of the method are described in [Zavada&Pířka \(2018\)](#), in this paper we will present only the result.

With the use of a second complementary method, we analyze distributions of angular separations of sources inside the 2D events (5). Distribution is generated from the set of events. We use either absolute separations

$$x_{ij} = |x_i - x_j|, \quad y_{ij} = |y_i - y_j|, \quad d_{ij} = \sqrt{x_{ij}^2 + y_{ij}^2}, \quad (10)$$

or the scaled ones

$$\hat{x}_{ij} = \frac{x_{ij}}{2\rho_2}, \quad \hat{y}_{ij} = \frac{y_{ij}}{2\rho_2}, \quad \hat{d}_{ij} = \frac{d_{ij}}{2\rho_2}, \quad (11)$$

Suitable unit of the parameters x_i, y_i, ρ_2 will be for our purpose $1 \text{ as } (1'')$. Distribution of scaled separations generated by Monte-Carlo (MC) for uniform distribution of stars in the sky is shown in Fig.3. The exact shape of normalized MC distributions reads

$$P(\hat{\xi}) = \frac{16\hat{\xi}}{\pi} \left(\arccos \hat{\xi} - \hat{\xi} \sqrt{1 - \hat{\xi}^2} \right); \quad \hat{\xi} = \hat{d}_{ij}, \quad (12)$$

$$P(\hat{\xi}) = \frac{64}{3\pi^2} \left((1 + \hat{\xi}^2) \text{EllipticE}(1 - \hat{\xi}^2) - 2\hat{\xi}^2 \text{EllipticK}(1 - \hat{\xi}^2) \right); \quad \hat{\xi} = \hat{x}_{ij}, \hat{y}_{ij}, \quad (13)$$

where the functions EllipticK (EllipticE) are complete elliptic integrals of the first (second) kind. The proof is given in Appendix A. These distributions do not depend on the event multiplicity and radius, this is an advantage of the scaled separations. Obviously, we have always $0 < \hat{\xi} < 1$. These exact functions replace their approximations resulting from MC calculation applied in the previous paper.

2.3. 3D methods

Similarly, as in the 2D case, we shall work with absolute separations

$$X_{ij} = |X_i - X_j|, \quad Y_{ij} = |Y_i - Y_j|, \quad Z_{ij} = |Z_i - Z_j|, \quad (14)$$

$$D_{ij} = \sqrt{X_{ij}^2 + Y_{ij}^2 + Z_{ij}^2}, \quad \Delta_{ij} = \sqrt{X_{ij}^2 + Y_{ij}^2}, \quad (15)$$

and/or with the scaled ones

$$\hat{X}_{ij} = \frac{X_{ij}}{2\rho_3}, \quad \hat{Y}_{ij} = \frac{Y_{ij}}{2\rho_3}, \quad \hat{Z}_{ij} = \frac{Z_{ij}}{2\rho_3}, \quad \hat{D}_{ij} = \frac{D_{ij}}{2\rho_3}, \quad \hat{\Delta}_{ij} = \frac{\Delta_{ij}}{2\rho_3}. \quad (16)$$

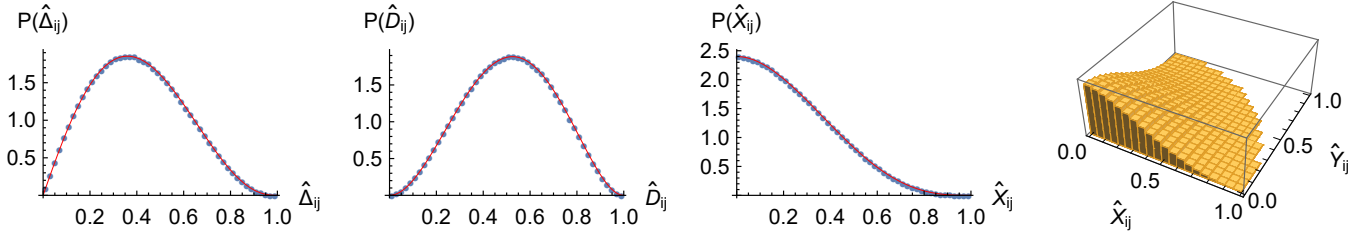


Figure 4. MC distributions of separations between uniformly generated stars (points) in 3D. The red curves represent functions (17) - (19). The Monte-Carlo statistics is represented by 5×10^5 events of multiplicity $M = 5$.

	2D region: $l \times b[\text{deg}^2]$	$\rho_2[as]$	$\langle L \rangle [\text{pc}]$	$\langle M \rangle$	N_e
N&S	$\langle -180, 180 \rangle \times \langle \pm 60, \pm 80 \rangle$	72	1290	3.21	2055674
C	$\langle 140, 180 \rangle \times \langle -10, 10 \rangle$	18	1912	2.75	3588183

Table 1. Analyzed regions in the DR2 catalogue, where ρ_2 is the angular radius of the events, $\langle L \rangle, \langle M \rangle$ are average distance and event multiplicity, N_e is the total number of events. Only sources in distance 1-5000pc are taken into account. The analysis is done for events $2 \leq M \leq 15$.

Suitable unit of the parameters X_i, Y_i, Z_i, ρ_3 is for our purpose 1pc. Distribution of scaled separations generated by MC from the uniform distribution of stars in 3D region of sky is shown in Fig.4. Exact shapes of these normalized MC distributions read

$$P(\hat{\xi}) = 12\hat{\xi}^2(2 - 3\hat{\xi} + \hat{\xi}^3); \quad \hat{\xi} = \hat{D}_{ij}, \quad (17)$$

$$P(\hat{\xi}) = \frac{9}{2}\hat{\xi} \left((2 + \hat{\xi}^2)\sqrt{1 - \hat{\xi}^2} + \hat{\xi}^2(4 - \hat{\xi}^2) \ln \frac{\hat{\xi}}{1 + \sqrt{1 - \hat{\xi}^2}} \right); \quad \hat{\xi} = \hat{\Delta}_{ij}, \quad (18)$$

$$P(\hat{\xi}) = \frac{12}{5}(1 - \hat{\xi})^3(1 + 3\hat{\xi} + \hat{\xi}^2); \quad \hat{\xi} = \hat{X}_{ij}, \hat{Y}_{ij}, \hat{Z}_{ij}, \quad (19)$$

as proved in Appendix A. Shapes of these distributions similarly to (12), (13) do not depend on event multiplicity and radius. The analysis with the use of characteristic functions $\Theta_n(M)$ could be in 3D case done separately in the plains XY, YZ and ZX . However, such analysis is not the aim of the present paper.

2.4. Aims

In Sec.3 using the DR2 data set we shall obtain the characteristic functions $\Theta_n(M)$, afterwards we check distributions (12) and (13). The distributions (17)–(19) will be used for the data analysis in Sec.4.1. All these distributions are of key importance for the analysis of real data. They represent the templates, which can reveal a violation of uniformity in the star distributions. Binary (and multiple) star systems are an example of such a violation, which manifests as the peaks in the distributions of angular or space separations in the region of close sources. In general, the scale of expected structure violating uniformity should be less than the event radius ρ_2 or ρ_3 .

3. ANALYSIS OF 2D EVENTS

Here we present the results obtained from regions of DR2 catalogue listed in Tab.1. The regions are shown in Fig.5. The corresponding events are created with the same angular radius as in Zavada&Piška (2018), which allows us the consistent comparison of results from the DR1 and DR2 catalogues. First, we checked the events covering the regions N&S. Their non-uniformity defined by the characteristic functions $\Theta_n(M)$ is demonstrated in Fig.6. The clear result $\Theta_n(M) > 1$ indicates the presence of clustering.

Corresponding distributions of angular separations are shown in Fig.7 together with curves (12), (13). These results can be compared with those in figures 7 (lower panels), 10 and 11 in the former paper. We observe:

i) The peaks at small angular separations in the DR2 corresponding to binaries are clearer, more pronounced than in the DR1 catalogue. Panels *e, k* in Fig.7 demonstrate the double stars separated by $d_{ij} \lesssim 0.5as$ are absent because such

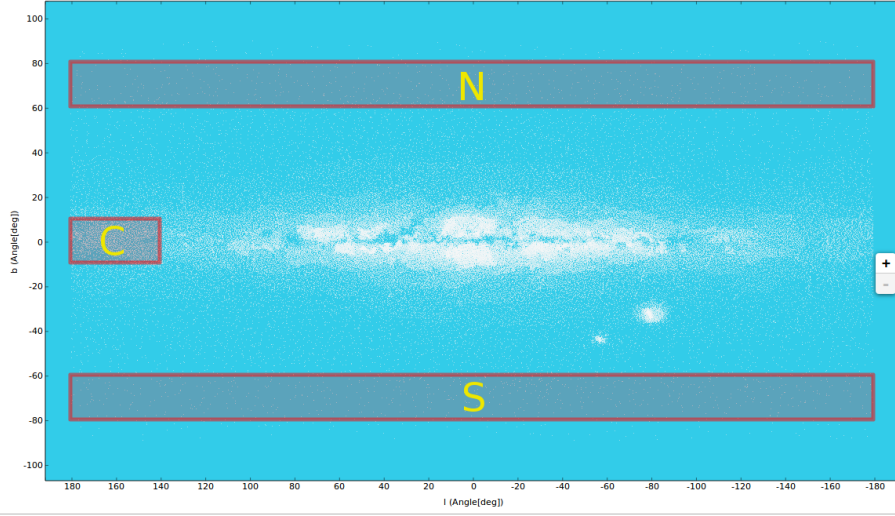


Figure 5. Analyzed regions in the DR2 catalogue.

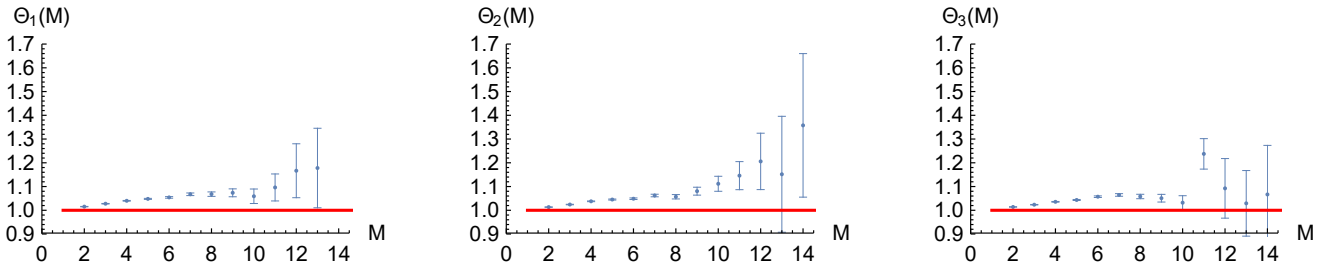


Figure 6. Characteristic functions $\Theta_n(M)$, $n = 1, 2, 3$ for events in the area N&S without any cut on magnitudes. Red line corresponds to the uniform distribution of sources.

close pairs are not resolved in the DR2 data set as reported in [Arenou \(2018\)](#). In both catalogues, we observe an excess of binaries in the region N&S for $\hat{d}_{ij} \lesssim 0.06$ or equivalently for $d_{ij} \lesssim 8.6as$. For greater separations inside the event, we observe perfectly uniform distributions of stars. Note the data and curves are equally normalized for $0 < \hat{\xi} < 1$. That is why the strong peak in panels g, h, i is balanced by a small reduction of distribution outside the peak. Brighter stars ($G \leq 15$, panels g, h, i, j, k, l) show evidently stronger peaks than sample without any cut on magnitude (panels a, b, c, d, e, f). A similar tendency was observed already in the catalogue DR1.

ii) More pronounced presence of binaries is demonstrated also in Fig.6. The slopes of lines in DR2 are greater than in DR1 - clustering is more obvious. For $M \leq 8$ the slopes are $\approx 4\%$ (8%) for the DR1(DR2) data. In Fig.8 we have shown some results obtained in a more populated region C. Also here we can observe a clear peak at small angular separations of sources of the magnitude $G \leq 15$, which proves the presence of binaries. Panel b again demonstrates the absence of double stars separated by $d_{ij} \left(\hat{d}_{ij} \right) \lesssim 0.5as$ (0.014) due to insufficient resolution. Different scales of \hat{d}_{ij} in Figs.7l and 8c are due to different radii ρ_2 of events from N&S and C regions. Similar plots could be presented for whole spectrum of magnitudes in the region C, however elevation above the red line due to binaries is much less than that in Fig.8c. The reason can be that denser region C with all magnitudes generates higher background of the optical doubles and a consequently lower relative rate of binaries.

4. BINARIES IN 3D EVENTS

We present the results obtained from 3D region defined in Tab.2. The parallax and angular components of the star proper motion are the parameters, which substantially enrich the recent Gaia data. We work with the 3D events (9).

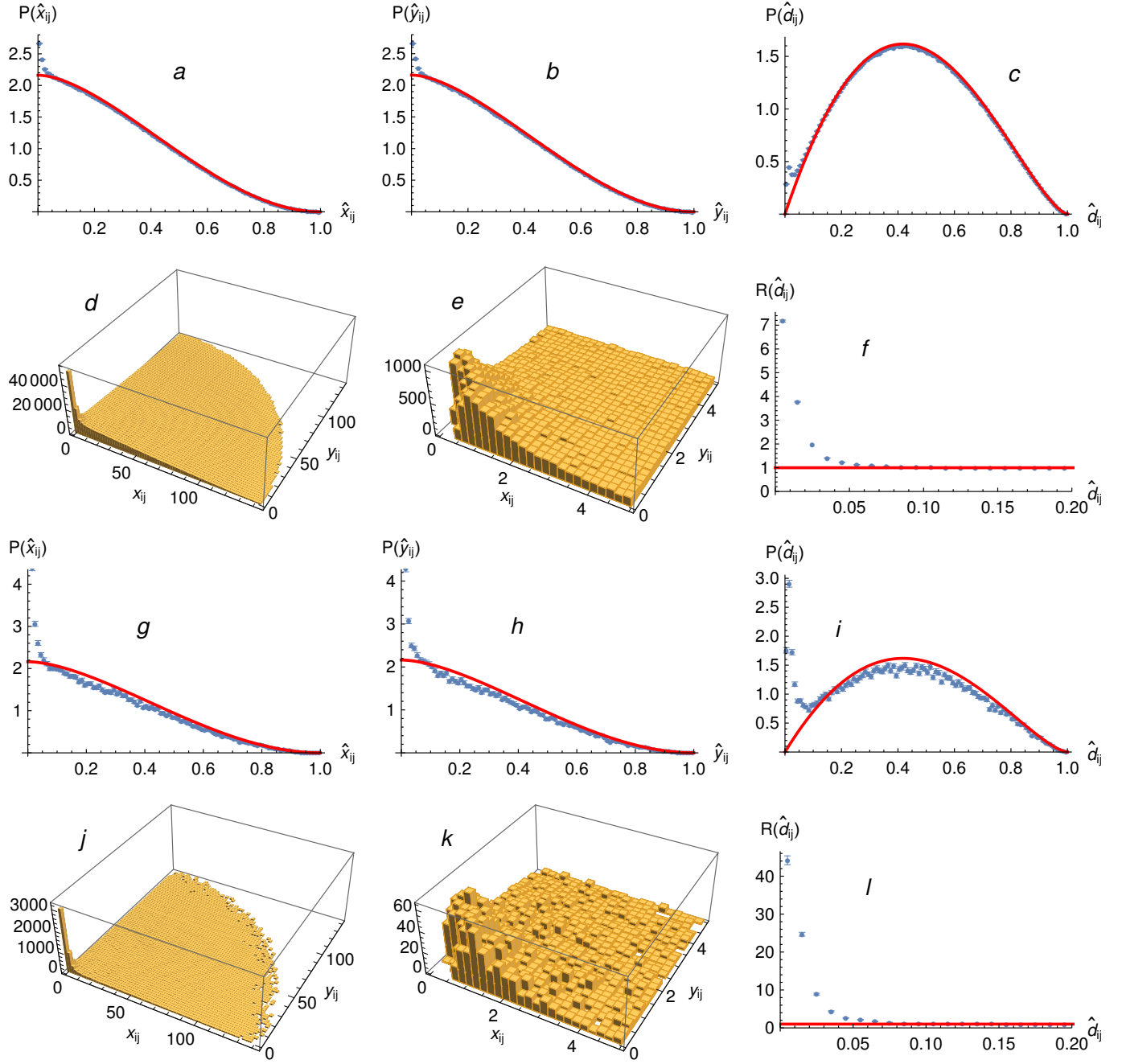


Figure 7. Panels *a,b,c,d,e,f*: distributions of angular separations in the region N&S for all G . The blue points in the panels *a,b* and *c* represent the data on scaled separations \hat{x}_{ij} , \hat{y}_{ij} , \hat{d}_{ij} and the red curves are functions (12), (13) representing uniform simulation. The panel *f* is the ratio of data to simulation from panel *c*. Panels *d* and *e* represent 3D plot of separations x_{ij} , y_{ij} in different scales (unit is $1as$). Panels *g,h,i,j,k,l*: the same for sources $G \leq 15$.

4.1. Analysis of 3D separations

The summary results of the analysis obtained from all magnitudes G are shown in Fig.9. Distributions of scaled separations in panels *a,b,c,g,h* perfectly match the uniform distribution of sources, but with exception of the first bin in *a,b,h*. Apparent excess of very close pairs in planes XY , YZ , ZX is seen also in panels *d,e,f*. However the sharp peak can be observed only in the plane XY (panel *d* and its magnified version *j*). Smearing in direction of Z (difference of radial positions, panels *c,e,f*) is due to lower accuracy in measuring of parallaxes. The errors of local coordinates

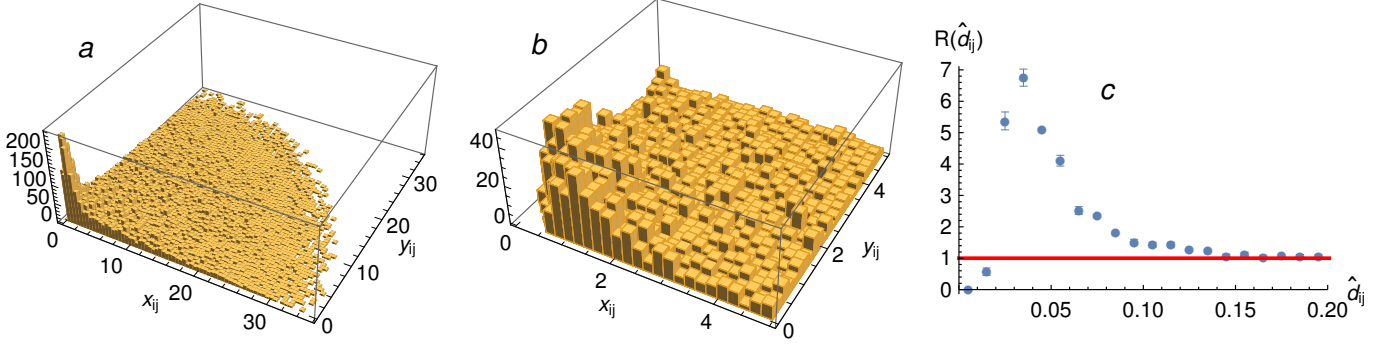


Figure 8. Panels *a,b,c*: distributions of angular separations in the region C for sources $G \leq 15$. Panels *a* and *b* represent 3D plot of separations x_{ij}, y_{ij} in different scales (unit is $1as$). Panel *c* is the ratio of data distribution $P(\hat{d}_{ij})$ to the function (12), like panels *f,l* in previous Fig. 7.

Region	ρ_3 [pc]	$\langle L \rangle$ [pc]	$\langle M \rangle$	N_e
cube of edge 400pc	2	188	6.8	727744

Table 2. Region of 3D analysis is cube centred at the origin of the galactic reference frame. Only sources of positive parallax are included. ρ_3 is the radius of events, $\langle L \rangle, \langle M \rangle$ are average distance and event multiplicity, N_e is the total number of events. The analysis is done for events $2 \leq M \leq 15$.

depend on the errors of separations and with the use of definitions (7) and (8) are calculated as

$$\begin{aligned} \delta X_{ij} &= \sqrt{\left(\frac{\partial X_{ij}}{\partial L_i} \delta L_i\right)^2 + \left(\frac{\partial X_{ij}}{\partial L_j} \delta L_j\right)^2} \\ &\approx \delta L \sqrt{(\mathbf{n}_i \mathbf{k}_l)^2 + (\mathbf{n}_j \mathbf{k}_l)^2} \leq \sqrt{2} \rho_3 \frac{\delta L}{L} \end{aligned} \quad (20)$$

and similarly

$$\delta Y_{ij} \leq \sqrt{2} \rho_3 \frac{\delta L}{L}, \quad \delta Z_{ij} \approx \delta L \sqrt{(\mathbf{n}_i \mathbf{k}_r)^2 + (\mathbf{n}_j \mathbf{k}_r)^2} \leq \sqrt{2} \delta L. \quad (21)$$

Note that $\delta L/L = \delta p/p$, where p is parallax. Obviously $\delta Z_{ij} \gg \delta X_{ij}, \delta Y_{ij}$ since $\mathbf{n}_i \mathbf{k}_l, \mathbf{n}_j \mathbf{k}_l \ll \mathbf{n}_i \mathbf{k}_r \lesssim 1$. That is why we prefer distributions of Δ_{ij} to D_{ij} for obtaining precise results. Maximum values of separations X, Y, Z is 4pc, which follows from the event radius $\rho_3 = 2pc$. The excess of close pairs is obvious most explicitly from the distribution of Δ_{ij} in panel *k* that represents a magnified version of *h*. The important ratio of the distribution $P(\Delta_{ij})$ to the uniform simulation (red curve in panel *h* rescaled to $\Delta_{ij} = 2\rho_3 \hat{\Delta}_{ij}$) is shown in logarithmic scale of Δ_{ij} in panel *i*.

The same distributions but for brighter sources $G \leq 15$ are shown in Fig.10. Similarly, as in the 2D case, the peaks are stronger for brighter sources and distributions outside the peaks confirm uniformity of the star distribution. Again due to equal normalization of data and red curves for $0 < \hat{\xi} < 1$ the strong peak in panels *g,h* is balanced by a small reduction of distribution beyond the peak. The excess of close pairs observed in both figures again convincingly indicates the presence of binaries.

For quantitative estimates, the important panels are *i*, which display the ratio data/simulation. This is more accurate than only displaying peaks with some undefined background. Panels *i* suggest that separations of binary systems in the analyzed region meet very approximately

$$\Delta_{ij} \lesssim 0.1 - 0.2pc. \quad (22)$$

We observe only a tail of distribution corresponding to more separated binaries. Closer pairs are absent due to the limited angular resolution in DR2 data. This result is compatible with the older data reported in Close et al. (1990). In Sec.5 a more discussion is devoted to the probability of the binary separation above this limit. We have checked

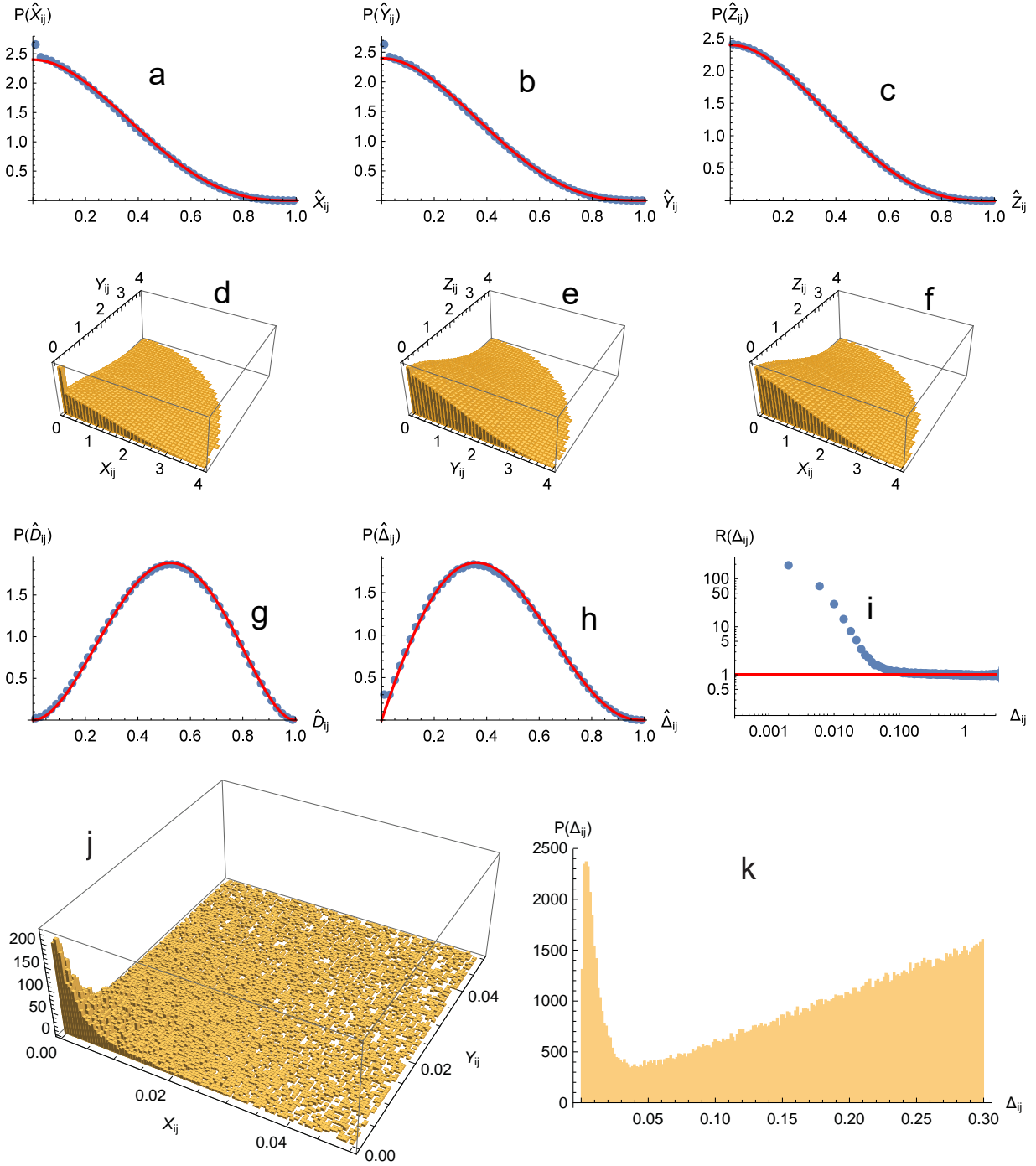


Figure 9. Distributions of separations (14-16) for all G . The blue points in the panels a, b, c, g and h represent the data on scaled separations $\hat{X}_{ij}, \hat{Y}_{ij}, \hat{Z}_{ij}, \hat{D}_{ij}, \hat{\Delta}_{ij}$ and the red curves are functions (17-19) representing uniform simulation. Panels (d, e, f) show 2D projections of separations. Panel (i) is the ratio of data to simulation from panel (h) . Panels (j, k) are magnified version of (d, h) . Unit of separations $X_{ij}, Y_{ij}, Z_{ij}, D_{ij}, \Delta_{ij}$ is 1pc.

that sampling with events generated by spheres of different radius ($\rho_3 = 5\text{pc}$) does not change the approximate result (22).

4.2. Proper motion of binaries

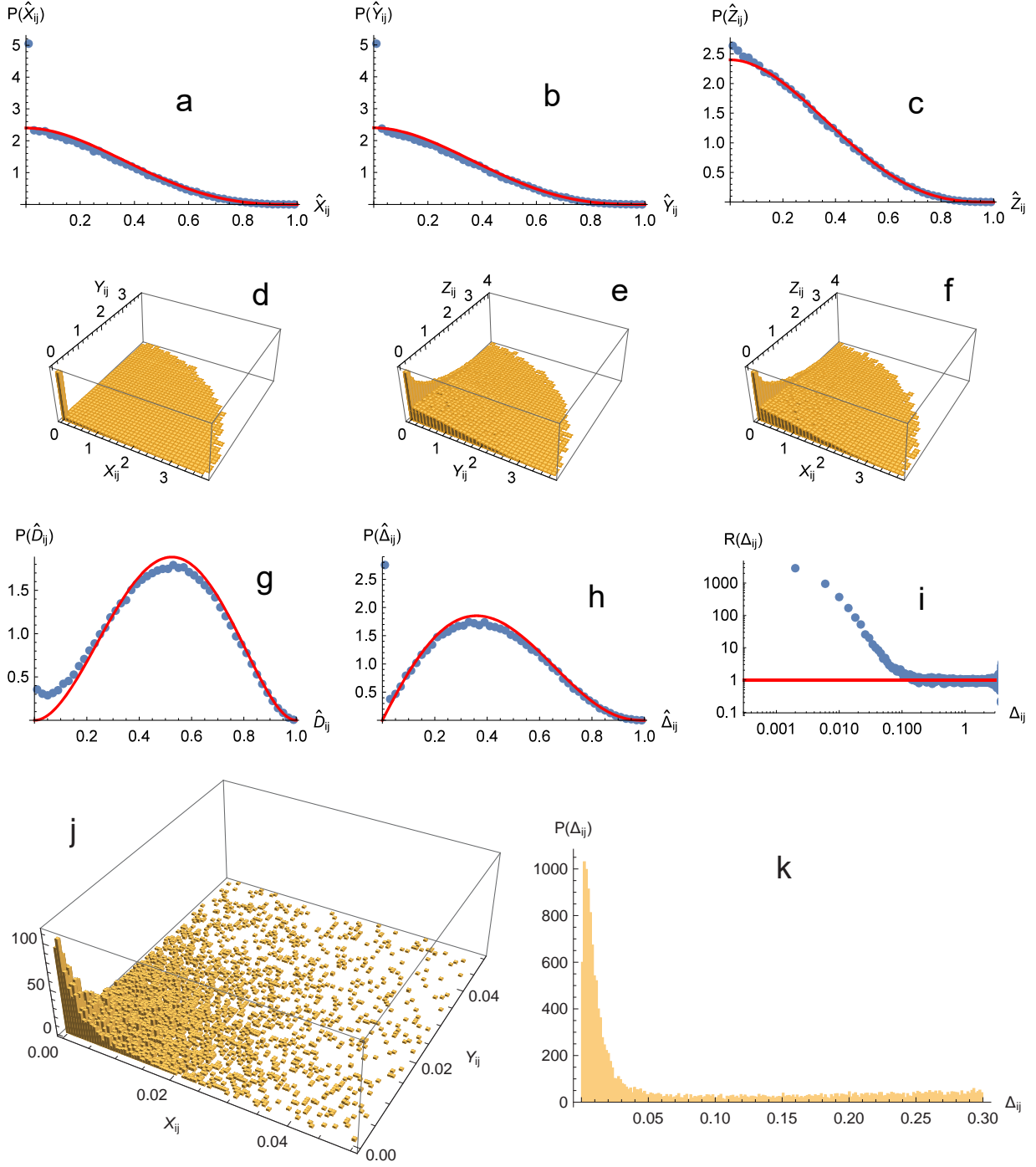


Figure 10. The same distributions as in the previous figure, but for bright pairs, $G \leq 15$.

The proper motion of the stars in DR2 is defined by two angular velocities

$$\mu_{\alpha*} (\equiv \mu_{\alpha} \cos \delta), \quad \mu_{\delta} \quad (23)$$

in directions of the right ascension and declination in the ICRS. So the corresponding transverse 2D velocity \mathbf{U} is given as

$$\mathbf{U} = L(\mu_{\alpha*}, \mu_{\delta}), \quad U = |\mathbf{U}|, \quad (24)$$

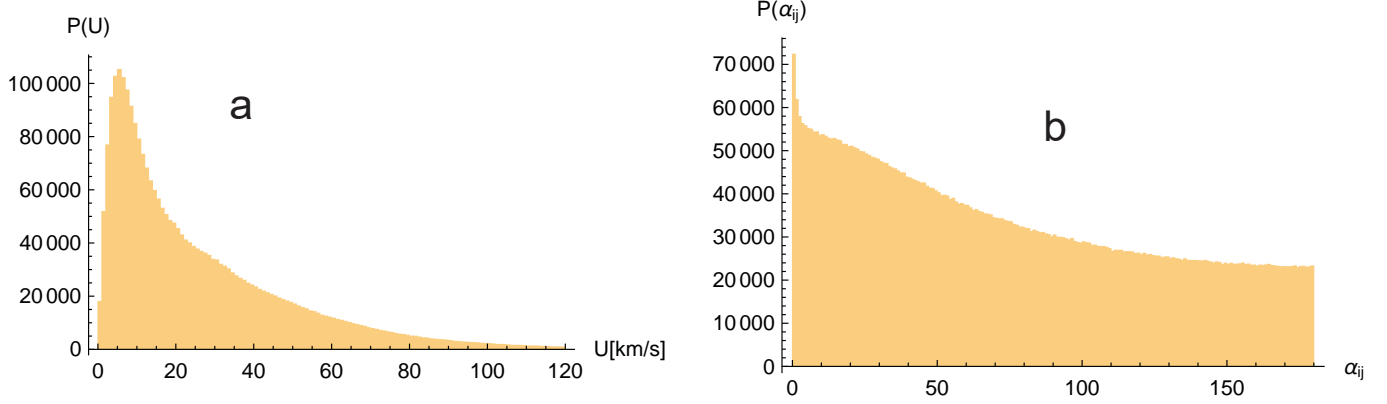


Figure 11. *Panel a:* Distribution of the star transverse velocities. *Panels b,c,d:* Distribution of the corresponding pair angles α_{ij} for $\Delta_{ij} > 0, 0.15$ and 1pc .

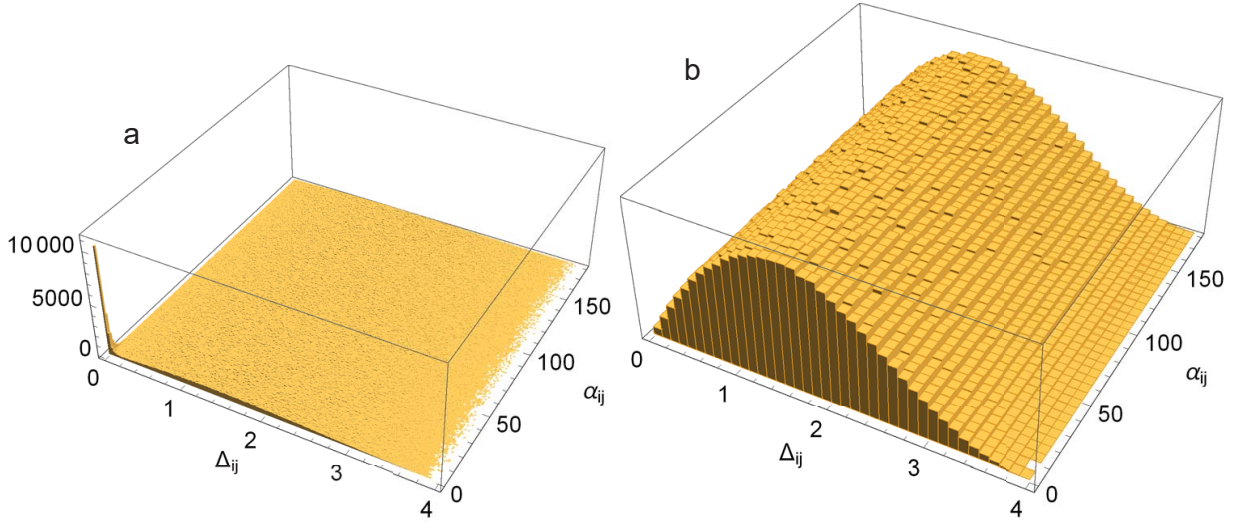


Figure 12. *Panel a:* Correlation of the pair transverse separation (unit is 1pc) with angle of corresponding transverse velocities. *Panel b:* Corresponding MC simulation generated from uniform distributions of positions and velocity directions.

where L is distance of the star calculated from the parallax (8). For the pair of stars we can define:

$$\alpha_{ij} = \arccos \frac{\mathbf{U}_i \cdot \mathbf{U}_j}{U_i U_j}, \quad U_{ij} = |\mathbf{U}_i + \mathbf{U}_j|, \quad v_{ij} = |\mathbf{U}_i - \mathbf{U}_j|, \quad (25)$$

where α_{ij} is angle between both transverse velocities. The corresponding errors read

$$\delta\alpha_{ij} \approx \sqrt{2} \frac{\delta u}{u}, \quad \delta U_{ij} = \delta v_{ij} \approx \sqrt{2} \delta u, \quad (26)$$

where

$$u = L\mu, \quad \delta u \approx u \sqrt{\left(\frac{\delta L}{L}\right)^2 + \left(\frac{\delta \mu}{\mu}\right)^2}. \quad (27)$$

Note that relative error $\delta v_{ij}/v_{ij}$ can be large, since v_{ij} is small compared with U_{ij} and the errors δv_{ij} and δU_{ij} are the same. In Fig.11a we show the distribution of the velocities U of the stars from the region defined in Tab.2. Distribution of the corresponding pair angles α_{ij} is presented in Fig.11b-d for different regions of Δ_{ij} . In Fig.12a we have shown the correlation of pair transverse separations and angles α_{ij} . We observe a very narrow peak in the region of small Δ_{ij}

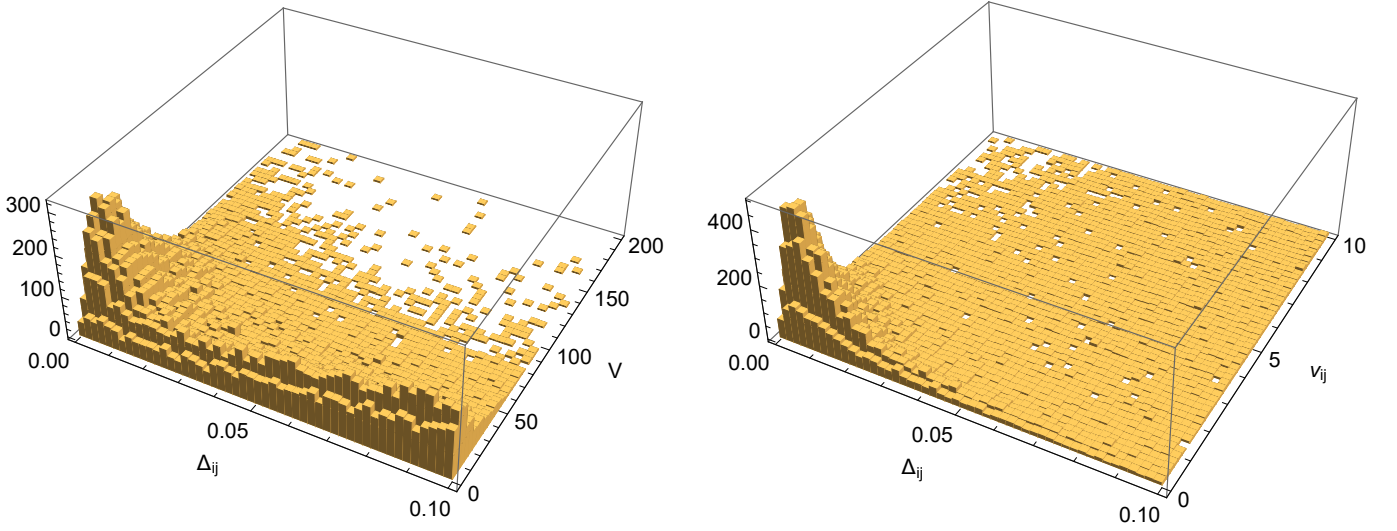


Figure 13. Correlation of the pair transverse separation Δ_{ij} with the transverse velocity V of the star system and with the transverse velocity v_{ij} of periodic motion. Unit of velocity is km/s.

and α_{ij} ¹. The peak is connected with presence of binaries as follows. The transverse velocities of two gravitationally coupled stars are

$$\mathbf{U}_i = \mathbf{V} + \mathbf{v}_i, \quad \mathbf{U}_j = \mathbf{V} + \mathbf{v}_j, \quad (28)$$

where \mathbf{V} is transverse velocity of their center of gravity and $\mathbf{v}_i, \mathbf{v}_j$ are transverse projections of instantaneous orbital velocities, they have always opposite direction. Dominance of very small α_{ij} means that

$$v_i = |\mathbf{v}_i| \ll |\mathbf{V}|, \quad (29)$$

so for binaries in our Δ window (Δ_{min} is given by resolution of two close sources and $\Delta_{max} = 0.1\text{pc}$ by (22)) we have

$$U_{ij} \approx 2V, \quad v_{ij} = v_i + v_j. \quad (30)$$

For comparison, we have generated MC plot from uniform distributions of positions and velocity directions, which is shown in Fig.12b. Obviously, uniform distribution contradicts to Fig.12a, which reflects the presence of binaries (peak at small α_{ij} and Δ_{ij}). The corresponding α_{ij} peak is also observed in Fig.11b-d on the background of collective motion of stars (dominance of $\alpha_{ij} < 90^\circ$). The peak is suppressed for $\Delta_{ij} \gtrsim 1\text{pc}$. Selection of comoving systems is a basis of the methodology applied in the catalogue JEC.

In Fig.13 we show correlations of the velocities V and v_{ij} with Δ_{ij} in the region of small separations, where the binaries are present. With the use of v_{ij} and Δ_{ij} will try to roughly estimate the orbital period of the binary star. To simplify the calculation, we assume the space binary orbits are circular and the star 3D separation is a (semi-major axis). There are the extreme cases:

A) $M_1 \approx M_2$, then

$$\mathbf{v}_i \approx -\mathbf{v}_j, \quad v_{ij} \approx v_i + v_j. \quad (31)$$

Orbital period is

$$T_A \approx \frac{\pi a}{w}, \quad (32)$$

¹ Input data (23) are related to the ICRS and Δ_{ij} is calculated in the galactic reference frame. Nevertheless the parameters $\Delta_{ij}, \alpha_{ij}, U_{ij}, v_{ij}$ are invariant under rotation.

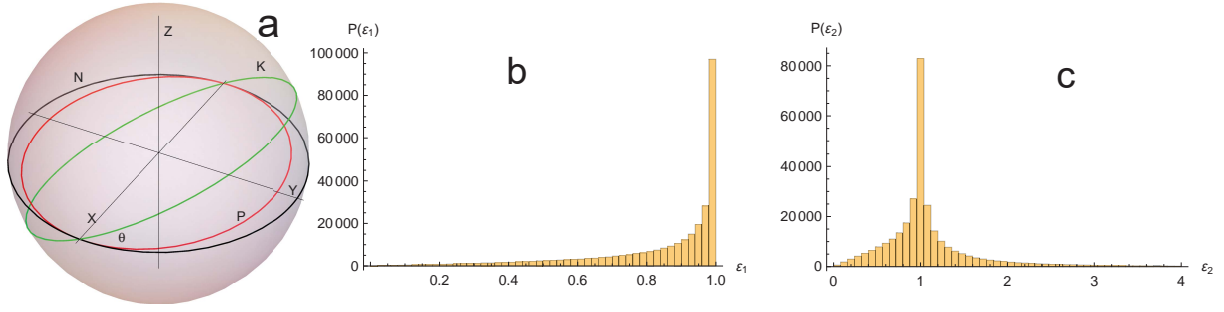


Figure 14. Panel a: Real orbit (K) and its deformed projection on the sky (P). Real orbit (N) in the plane xy . Panels b,c: Distributions of random parameters ε_1 and ε_2 .

where w is the space orbital velocity and a equals to the diameter of the orbit.

B) $M_1 \gg M_2$, then

$$v_2 \approx 0, \quad v_{ij} \approx v_1, \quad (33)$$

but the orbital period is different

$$T_B \approx \frac{2\pi a}{w}, \quad (34)$$

since the separation a equals to the orbit radius.

At the same time, Kepler's law implies for orbital period T_g :

$$T_g = 2\pi \sqrt{\frac{a^3}{GM_{tot}}}, \quad (35)$$

where G is gravitational constant and $M_{tot} = M_1 + M_2$ is mass of the star system. For units T_g [y], a [pc] and M_{tot} [M_\odot] we have

$$T_g = 0.937 \times 10^8 \sqrt{\frac{a^3}{M_{tot}}}. \quad (36)$$

This relation also allows us to estimate the period. If the plane of orbit is perpendicular to the line of sight (axis Z), like the orbit N in Fig.14a, then it is possible to simply substitute:

$v_{ij}/2 \rightarrow w$, in (32), $v_{ij} \rightarrow w$, in (34) and $\Delta_{ij} \rightarrow a$ in (36), (32), (34).

Then we get:

$$T_g = 0.937 \times 10^8 \sqrt{\frac{\Delta_{ij}^3}{M_{tot}}}, \quad T_v = T_A = T_B = \frac{2\pi \Delta_{ij}}{v_{ij}}. \quad (37)$$

The orbit reference frame in figure is similar to the local 3D event frame defined by the basis (2) and coordinates (7). But its origin \mathbf{L}_0 is defined by the actual position of the centre of mass of the binary. How to deal with the orbits, whose plane is not perpendicular to the line of sight like the orbit K in the same figure? The orbits in the figure are defined as follows:

$$\begin{aligned} N : X &= r \cos \phi, & Y &= r \sin \phi, & Z &= 0 \\ K : X &= r \cos \phi \cos \theta, & Y &= r \sin \phi, & Z &= r \cos \phi \sin \theta \\ P : X &= r \cos \phi \cos \theta, & Y &= r \sin \phi, & Z &= 0 \end{aligned}$$

where $r = a/2$ for the case A, $r = a$ for B and ϕ is azimuthal angle in the plane XY . The orbit K inclined at an angle θ is observed only in its projection P . Corresponding observed separation between the stars is Δ_{ij} :

$$a \rightarrow \Delta_{ij}, \quad \sqrt{a^3} \rightarrow \sqrt{\Delta_{ij}^3} = \sqrt{a^3} \varepsilon_1, \quad \varepsilon_1 = (\cos^2 \phi \cos^2 \theta + \sin^2 \phi)^{3/4}. \quad (38)$$

Random angles ϕ, θ generate distribution of ε_1 shown in Fig.14b. The MC distribution demonstrates smearing of the real separation a due to random ϕ and slope θ of the orbit. Similarly, the ratio a/w is distorted as

$$\frac{a}{w} \rightarrow \frac{\Delta_{ij}}{v_{ij}} = \frac{a}{w} \varepsilon_2, \quad \varepsilon_2 = \frac{\sqrt{\cos^2 \phi \cos^2 \theta + \sin^2 \phi}}{\sqrt{\sin^2 \phi \cos^2 \theta + \cos^2 \phi}}. \quad (39)$$

Since velocity \mathbf{w} is perpendicular to \mathbf{r} , there is exchange $\cos^2 \phi \leftrightarrow \sin^2 \phi$ in denominator. Corresponding distribution of ε_2 is shown in Fig.14c. The mean values are

$$\langle \varepsilon_1 \rangle = 0.791, \quad \langle \varepsilon_2 \rangle = 1.21$$

and represent a scale of distortion of real orbital periods, if replaced by relations (37). More accurate estimate of the periods in some region of Δ_{ij} can be obtained by rescaling of these relations:

$$\langle T_v \rangle = \frac{2\pi}{\langle \varepsilon_2 \rangle} \left\langle \frac{\Delta_{ij}}{v_{ij}} \right\rangle, \quad \langle T_g \rangle = \frac{0.937 \times 10^8}{\langle \varepsilon_1 \rangle \sqrt{M_{tot}}} \left\langle \sqrt{\Delta_{ij}^3} \right\rangle. \quad (40)$$

We have estimated the average periods from the maximum in Fig.13. If we take the sources roughly in the region of half-width of the maximum,

$$\Delta \leq 0.015 \text{pc}, \quad v_{ij} \leq 1.5 \text{km/s}, \quad (41)$$

then

$$\langle T_v \rangle \approx 8.0 \times 10^4 \text{y} \quad (42)$$

and one can check that equality $\langle T_v \rangle = \langle T_g \rangle$ implies estimation $M_{tot} \approx 0.8 M_\odot$.

5. DISCUSSION

The separation of a pair of stars and the similarity of their movements can serve as two signatures of the binaries. We can compare them:

i) Distributions of the 2D and 3D separations are studied in Sec.3 and 4.1. The procedure is simple, the distribution of separations $P(\Delta)$ (within the defined circles or spheres) is compared with the corresponding separations $P_{bg}(\Delta)$ generated by uniformly distributed sources representing background

$$P_{bg}(\Delta) d\Delta = N_{bg} P_0(\hat{\xi}) d\hat{\xi}; \quad 2\rho\hat{\xi} = \Delta = d_{ij} \text{ or } \Delta_{ij}, \quad (43)$$

where P_0 is given by (12) or (18) and N_{bg} is the corresponding number of the background pairs in the data events. Its accurate calculation is described below, see Eqs. (47)-(49). The binary distribution reads

$$P_{bin}(\Delta) = P(\Delta) - P_{bg}(\Delta)$$

and the probability $\beta(\Delta)$ that the pair is a real binary is given as

$$\beta(\Delta) = \frac{P_{bin}(\Delta)}{P(\Delta)} = 1 - \frac{P_{bg}(\Delta)}{P(\Delta)}. \quad (44)$$

The function $R(\Delta)$ displayed in Figs. 7f, 7l, 8c, 9i and 10i is another representation of the probabilistic function $\beta(\Delta)$:

$$R(\Delta) \approx \frac{1}{1 - \beta(\Delta)}. \quad (45)$$

Consider the distribution $P(\Delta)$ from Figs.9k and 10k. The corresponding function $\beta(\Delta)$ is shown in Fig.15a, where the red curve represent fit of the function:

$$\beta(\Delta) = \omega \exp\left(-\frac{\Delta^2}{2\sigma_2^2}\right) + (1 - \omega) \exp\left(-\frac{\Delta}{\sigma_1}\right). \quad (46)$$

The result of the fit is shown in the first row (all pairs) of Tab.3. The longer tail corresponding to the second term describes the small probability of bound pair at greater separations: $\Delta \gtrsim 0.15 \text{pc}$. This tail is not visible in panels *i* in Figs. 9 and 10. Two exponential terms in $\beta(\Delta)$ may correspond to two different classes of binaries. The question is to what extent the excess of wide binaries consists of stable bound systems. Part of the excess may be an image of widening pairs that were less separated but weakly bound in the past. The accuracy of the method is based on three conditions:

- precise separation measurement in a suitably selected statistical set of events that generates $P(\Delta)$
- precise modelling of the background defining $P_{bg}(\Delta)$

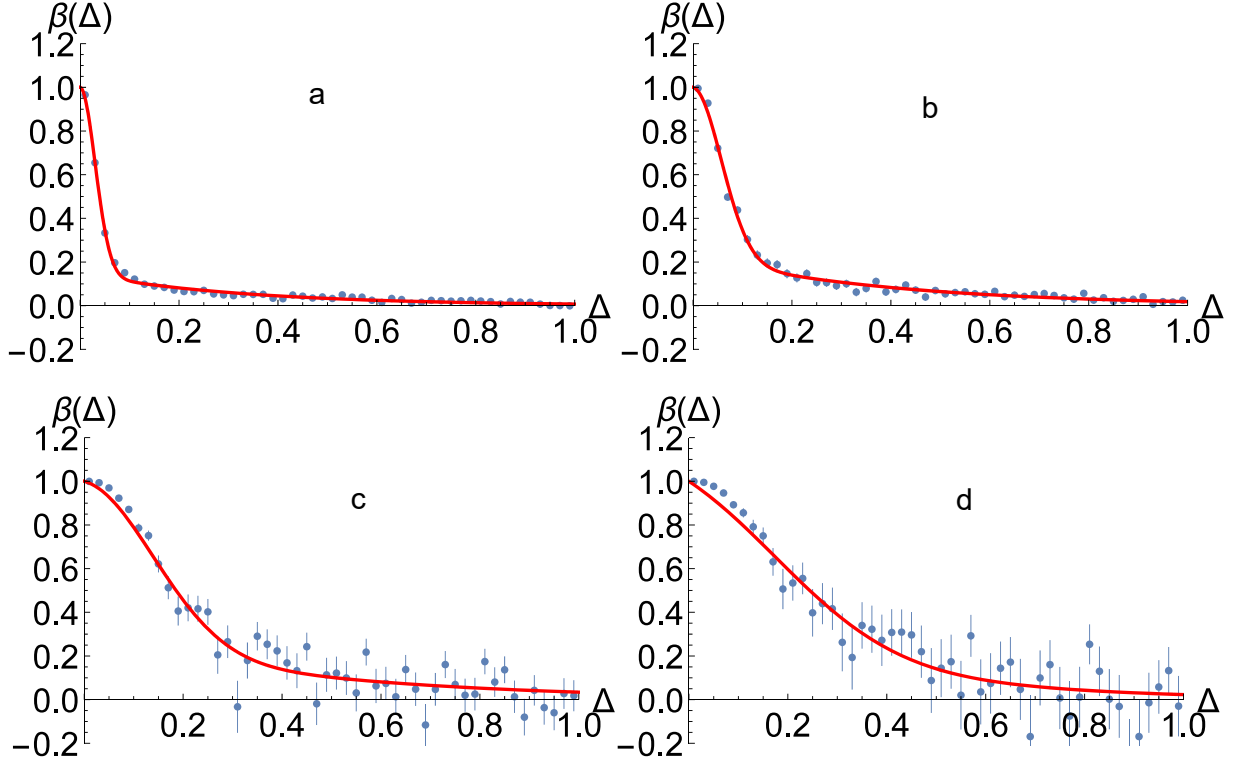


Figure 15. Probabilistic function $\beta(\Delta)$ for different domains $\Delta \times \alpha$ and intervals of magnitude G . *Panel a:* all pairs and magnitudes. *Panels b, c, d:* united domain **AB** for magnitude intervals G all, $G \leq 15$, $G \leq 13$. Blue points with error bars are data, red curves are fits (46).

	ω	$\sigma_1[pc]$	$\sigma_2[pc]$
all pairs	0.852	0.335	0.0303
all pairs and domain AB	0.771	0.396	0.0573
$G \leq 15$ and domain AB	0.705	0.464	0.143
$G \leq 13$ and domain AB	0.505	0.326	0.215

Table 3. Values of the parameters $\omega, \sigma_1, \sigma_2$.

- relatively high peak and low background giving probability $\beta(\Delta)$ close to 1 in the peak region.

ii) In principle, a similar approach could be applied to comoving pairs. However, it is obvious the meeting the conditions above is more difficult for velocities or their differences. The precision of velocity measurement is lower than separation. The distribution of velocities is far from being simply uniform, we do not know the exact form of the velocity background. Fig.11b suggests a more complicated collective motion in the background and a relatively low peak of binaries. That is why we prefer the primary signature based on the spatial separation, where we work with exactly defined background and relatively high peaks, like panels i, k in Figs.9 and 10. On the other hand, one can expect that a combination of position and velocity data will suppress background and improve the selection of binaries in terms of the function $\beta(\Delta)$. A selection based on such a combination is described below. In Sec.4.2 we have shown that combination of the space separation with proper motion allows us to estimate the orbital period.

We denote by N_{bin}^D and N_{bg}^D the numbers of real and false (background) binaries in some domain D of separations Δ . Correspondingly we denote $N_2^D = N_{bin}^D + N_{bg}^D$, where N_2^D is the number of pairs in given dataset. We have

$$N_{bg}^D = \int_D P_{bg}(\Delta) d\Delta, \quad (47)$$

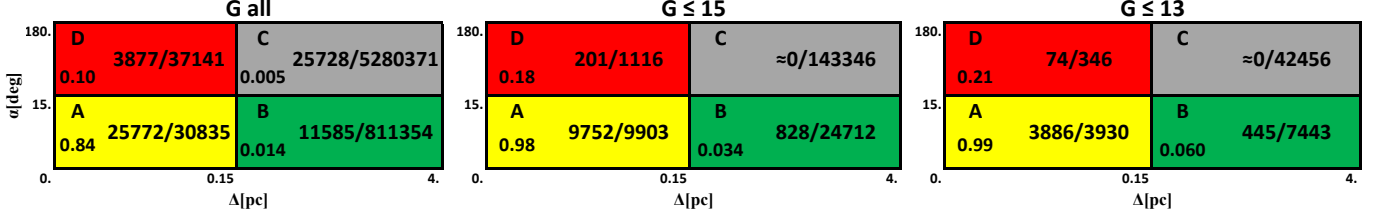


Table 4. The ratio N_{bin}/N_2 of the number of binaries and the total number of pairs in different domains $\Delta \times \alpha$ and intervals of magnitude G .

		N_s	N_{bin}	N_{bin}/N_s
<i>all</i>	G	2734222	66962	0.024
	$G \leq 15$	474689	10781	0.023
	$G \leq 13$	256787	4405	0.017

Table 5. The number of binaries N_{bin} with the total number of sources N_s in different intervals of the magnitude G .

where P_{bg} is distribution defined by (18) and renormalized in such a way that

$$\int_E P_{bg}(\Delta) d\Delta = \int_E P(\Delta) d\Delta \quad (48)$$

where the integration is over the domain E safely outside the peak of binaries. So we calculate

$$N_{bg}^D = N_2^E \frac{\int_{D(\Delta)} P_0(\Delta) d\Delta}{\int_{E(\Delta)} P_0(\Delta) d\Delta}, \quad (49)$$

where P_0 is defined by (18) with the substitution $\hat{\xi} = \Delta/2\rho$. The same procedure can be applied for the domains $D(\Delta) \times D(\alpha)$. Since we can assume that Δ and α are not correlated in the background distribution

$$P_{bg}(\Delta, \alpha) \approx P_0(\Delta) P(\alpha), \quad (50)$$

then

$$N_{bg}^D = N_2^E \frac{\int_{D(\Delta)} P_0(\Delta) d\Delta \int_{D(\alpha)} P(\alpha) d\alpha}{\int_{E(\Delta)} P_0(\Delta) d\Delta \int_{E(\alpha)} P(\alpha) d\alpha}. \quad (51)$$

If we choose $D(\alpha) = E(\alpha)$, then the second ratio is 1. In this way, we can calculate N_{bg}^D without the knowledge of $P(\alpha)$. The selected domains are shown, together with the results $\beta \approx N_{bin}/N_2$ in Tab.4. For the calculation, we take the common interval $E(\Delta) \equiv \langle 2, 4 \rangle \text{pc}$, where N_{bin}^E should be zero. In an accordance with Fig.12a we observe the highest rate of binaries in the domain **A** $\equiv \langle 0, 0.15 \rangle \text{pc} \times \langle 0, 15 \rangle \text{deg}$. The binaries are well observable also in the neighbouring domain **B** $\equiv \langle 0.15, 4 \rangle \text{pc} \times \langle 0, 15 \rangle \text{deg}$. For $G \leq 15$ the number of binaries in the domains **C** is zero within statistical errors. Presence of binaries in the domain **D** requires further analysis.

The probabilistic function $\beta(\Delta)$ corresponding to the united domain **AB** is shown in panels *b, c, d* in Fig.15 for different intervals of the magnitude G . Obviously, the function (46) fitted with the parameters listed in Tab.3 can be rather approximate. We observe the function β is getting wider with decreasing G . This may suggest that brighter and therefore statistically more massive stars can form stable bound systems even at greater separations. Obviously, for $\Delta \gtrsim 1 \text{pc}$, the probability β is compatible with zero. This also corresponds to an absence of a binary peak in Fig.11d, which relates to $\Delta > 1 \text{pc}$. Total numbers of binaries are listed in Tab.5. The results suggest that in the Gaia DR2 data in the region defined by Tab.2, the number of binaries can represent $\approx 2\%$ of all stars in this region.

6. CATALOGUE

In this section, we describe the catalogue of binary candidates, which we have created from the events of multiplicity $2 \leq M \leq 15$ defined by Tab.2. For the first version of the catalogue we accept only the candidates from domain **A** shown in the first panel in Tab.4. So, we do not accept all candidates, but only candidates with a high probability to be the true binary. The candidates meet the following conditions:

1) Projection of separation

We accept the pairs, which satisfy

$$\Delta_{cat} \leq 0.15 \text{ pc.} \quad (52)$$

In general, the projection of separation Δ depends on the reference frame. In the paper, we worked with the local reference frame defined by the event centre, where projection Δ into the local plane XY is given by (15). In the catalogue we do not use local frames. The cut (52) is applied to Δ_{cat} , which is defined as the length of the arc

$$\Delta_{ij,cat} = \frac{1}{2} (L_i + L_j) \arccos \mathbf{n}_i \mathbf{n}_j, \quad (53)$$

where $L_\alpha, \mathbf{n}_\alpha$ are defined in section 2.1. The separations Δ and Δ_{cat} are not exactly equal, but we have checked that in our conditions their difference is small, $\langle \delta \Delta \rangle \approx 0.007 \text{ pc}$. Then the sharp cut on Δ_{cat} means only a slightly smeared cut of the distribution of Δ .

2) Projection of collinearity

The pairs must meet the condition

$$\alpha \leq 15 \text{ deg.} \quad (54)$$

Both conditions define the domain **A** in the first panel of Tab.4. The panel shows that the average probability of a binary star is $\beta \approx 84\%$. If the stars are brighter, (second and third panel), then the average β is almost 100%.

3) Radial separation

In fact, the radial separation is not explicitly used in our algorithm of selection of binaries. The reason is a rather low precision of radial separations, as explained in the comments to Figs. 9 and 10. The only constraint is given by the diameter of our events (4pc). Separation selection is based solely on Δ_{ij} . Additional cuts on inaccurate radial separation would eliminate many of real binaries and invalidate the function β calculated for Δ_{ij} . We obtained high β even without a cut on radial separation.

Further, it is evident that spherical events fill the space only partially ($\approx 52\%$). In this way, half the stars is lost for analysis. We also lose binaries between two adjacent events when each star falls into another. In order to recover these losses, we work with the modified coverage:

i) The event spheres are replaced by cubes of edge 4pc with no gaps between them. In each cube, we search for the pairs meeting the conditions (52) and (54).

ii) The procedure is repeated with the same cubes centred in the corners of the former cubes and the search results are merged.

The catalogue is represented by a matrix that is defined as follows. Each line represents one star and there are the following data in the columns:

1–2: Group ID and Group size ($n \geq 2$) to match stars with the group they belong to².

3–96: Copy of the original entry for the star from Gaia-DR2 archive³, according to the documentation⁴.

97–98: Minimum and maximum angular separation of the star from other stars in the group [as].

99–100: Minimum and maximum projected physical separation of the star from other stars in the group [pc].

The summary data from our catalogue of binary candidates (I), along with the data extracted from the catalogue JEC - Jiménez-Esteban et al. (2019) (II) is shown in Tab.6. The number of candidates N_2 in this table correspond to N_2 in the domains **A** in Tab.4 after increasing with the repeated covering. The comparison of the two catalogues shows the following:

a) We can only compare sources of magnitude $G \leq 13$, because (II) does not contain less bright stars. Of the total number 3055 binaries in (II), only 301 lie in the (I) cube (400pc)³. Increasing the edge of this cube by the factor 2.15 would increase volume 10 times with the number of binaries comparable to the total (II).

² In the current version of our catalogue we omit candidates of systems $n > 2$, so only binaries ($n = 2$) are written.

³ http://cdn.gea.esac.esa.int/Gaia/gdr2/gaia_source/csv/

⁴ http://gea.esac.esa.int/archive/documentation/GDR2/Gaia_archive/chap_datamodel/sec_dm_main_tables/sssec_dm_gaia_source.html

Catalogue	N_2	(N_{bin})	G
(I): domain A	80560	(67670)	<i>all</i>
	22674	(22201)	≤ 15
	9082	(8991)	≤ 13
(II): total $N_{bin} = 3055$		(301)	≤ 13

Table 6. Summary table of binaries from the catalogues (I) and (II), see text. N_2 is the number of binary candidates, N_{bin} is the real expected number of binaries. The data in second column are related to the full cube region $(400\text{pc})^3$ (Tab.2).

b) The number 301(II) could be compared with the corresponding number of candidates $C_2 = 9082$ (I). However, in the JEC catalogue, apart from the cut $G \leq 13$ many other restrictions and selections are made. Definition of the binary is not the same in both catalogues. In our opinion, this is the reason for the difference between (I) and (II).

c) (I) and (II) have 108 common binary candidates.

d) 86(II) candidates are absent in (I) since the separation Δ exceeds 0.15pc. These candidates do not contradict to our general criteria, but the corresponding probability $\beta(\Delta)$ can be lower as shown in Fig.15.

e) 54(II) candidates are absent in (I) since their spatial separation exceeds 4pc (event diameter). Such candidates may not contradict to our criteria, however $\beta(\Delta)$ due to a great background can be extremely low.

f) 18(II) candidates are absent in (I) since these candidates are located in a dense area generating the high multiplicity events, which exceed our currently set limit.

g) The last 35(II) candidates are absent in (I), mainly due to the fact that even after the second coverage some couples (II) remain separated in two neighbouring event cubes.

The total number of the binary candidates of all Gaia magnitudes in the catalogue (I) is 80560, which corresponds to the expected real number of binaries 67670. The full current catalogue (I) in the csv form is available on the website <https://www.fzu.cz/~piska/Catalogue/>. We plan to further develop and optimize our catalogue methodology.

7. SUMMARY AND CONCLUSION

We have proposed a general statistical method for analysis of finite 2D and 3D patterns. In the present study, the method has been applied to the analysis of binary star systems in different regions of the Gaia catalogue DR2.

Results on 2D statistical analysis were compared with our former results obtained from the previous catalogue DR1. The new results give in the distribution of angular separations more clear evidence of binaries. Independent signature follows from the characteristic functions $\Theta_n(M)$, which clearly indicate a tendency to clustering. However, the most important results are obtained from the 3D analysis introduced in the present paper. We have analyzed about 5×10^5 of events inside the cube of edge 400pc centred at the origin of the galactic reference frame. In distributions of pair separations, we observe the sharp peaks at small separations corresponding to binaries, which are more striking for brighter sources, $G \leq 15$.

The important result of the analysis is probabilistic function $\beta(\Delta)$, which depends on the separation Δ of a pair of stars and indicates the probability that the pair constitutes a bound system. The function suggests that brighter, more massive binary stars have on average a greater separation. With increasing separation the function falls rapidly. We obtained the ratio binaries/singles $\approx 2\%$.

Further, we had shown that a combined analysis of 3D separations with the proper motion of the pairs of sources gives a clear picture of the binaries with two components of the motion: parallel and orbital. The analysis allowed us to estimate the average orbital period and mass of the binary star system in the chosen statistical ensemble.

The highest probability of the binary is observed at smallest separations Δ and angles α between proper motions. From the corresponding domain $\Delta \times \alpha \equiv \langle 0, 0.15 \rangle \text{pc} \times \langle 0, 15 \rangle \text{deg}$, we have created the catalogue involving 80560 binary candidates, which represents 67670 of the true binaries.

APPENDIX

A. PROOF OF RELATIONS (12), (13), (17), (18) AND (19)

i) Relation (12)

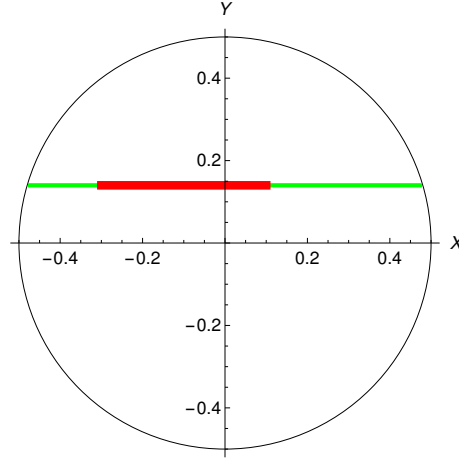


Figure 16. Random segment l (red) on the chord $L(y)$ (green).

First we consider two random points on a segment L . The probability that the points are separated by interval l reads:

$$p(l) \sim L - l. \quad (\text{A1})$$

Further, we suppose a circle of diameter $2R = 1$ with a chords $L(y)$ involving random segment l (Fig.16). We have

$$L(y) = 2\sqrt{(1/2)^2 - y^2} = \sqrt{1 - (2y)^2}. \quad (\text{A2})$$

The probability of interval l reads

$$P_{\parallel}(l) \sim \int_0^{y_{\max}} (L(y) - l) dy \sim \left(\arccos l - l\sqrt{1 - l^2} \right); \quad (\text{A3})$$

$$y_{\max} = \frac{1}{2}\sqrt{1 - l^2}, \quad 0 < l < 1.$$

This distribution is generated by random pairs on the chords parallel to axis x . For arbitrary random pairs separated by l inside the circle, we integrate distributions (A3) over all directions in 2D and replace

$$dl \rightarrow d(\pi l^2) \sim l dl, \quad (\text{A4})$$

which gives distribution

$$P_{\parallel}(l)dl \rightarrow P(l)dl \sim P_{\parallel}(l)l dl, \quad 0 < l < 1. \quad (\text{A5})$$

Relation (12) is its normalized form.

ii) Relation (13)

Distribution (A5) can be modified

$$P(l)dl \sim P_{\parallel}(l)l dl \sim P_{\parallel} \left(\sqrt{l_x^2 + l_y^2} \right) dl_x dl_y. \quad (\text{A6})$$

Calculation of integral

$$P(l_x) \sim \int_0^{l_{y\max}} P_{\parallel} \left(\sqrt{l_x^2 + l_y^2} \right) dl_y, \quad l_{y\max} = \sqrt{1 - l_x^2} \quad (\text{A7})$$

with the use of [Mathematica \(2018\)](#) and after replacement $l_x \rightarrow \hat{\xi}$ and normalization gives relation (13).

iii) Relation (17)

Now instead of circle $2R = 1$, we consider the sphere of the same radius. The procedure is a modification of the case i). Now instead of integral (A3) we get

$$P_{\parallel}(l) \sim \int_0^{y_{\max}} y (L(y) - l) dy \sim \left(\frac{1}{3} - \frac{l}{2} + \frac{l^3}{6} \right); \quad (\text{A8})$$

$$y_{\max} = \frac{1}{2}\sqrt{1 - l^2}, \quad 0 < l < 1,$$

where y means radius of a cylinder of parallel chords. The additional y in the integral means that we integrate chords on surfaces of cylinders of different radii. Then instead of (A4) we use

$$dl \rightarrow d\left(\frac{4}{3}\pi l^3\right) \sim l^2 dl, \quad (\text{A9})$$

since the integration of chords is over all directions in 3D. Resulting distribution reads

$$P(l)dl \sim P_{\parallel}(l)l^2 dl \sim l^2 \left(\frac{1}{3} - \frac{l}{2} + \frac{l^3}{6}\right), \quad (\text{A10})$$

which after normalization gives relation (17).

iv) Relation (19)

Probability $\mathbf{P}(l)$ of random segments $l = \sqrt{l_x^2 + l_y^2 + l_z^2}$ inside the sphere can be expressed as

$$\mathbf{P}\left(\sqrt{l_x^2 + l_y^2 + l_z^2}\right) dl_x dl_y dl_z \sim \mathbf{P}(l) l^2 dl \sim P(l) dl, \quad (\text{A11})$$

which together with (A10) gives

$$\mathbf{P}\left(\sqrt{l_x^2 + l_y^2 + l_z^2}\right) = \mathbf{P}(l) \sim \left(\frac{1}{3} - \frac{l}{2} + \frac{l^3}{6}\right). \quad (\text{A12})$$

The probability that segment l has projection l_x is given as

$$P(l_x) \sim \int_0^{l_{z\max}} \int_0^{l_{y\max}} \mathbf{P}\left(\sqrt{l_x^2 + l_y^2 + l_z^2}\right) dl_y dl_z \quad (\text{A13})$$

$$\sim \int_0^{t_{\max}} \mathbf{P}\left(\sqrt{l_x^2 + t^2}\right) t dt; \quad t_{\max} = \sqrt{1 - l_x^2}. \quad (\text{A14})$$

The last integral (equally for l_y, l_z) can be after inserting from (A12) easily calculated, and after normalization gives relation (19).

v) Relation (18)

In a similar way, the probability that segment l has projection $\Delta = \sqrt{l_x^2 + l_y^2}$ is given as

$$P(\Delta) \sim \int_0^{l_{z\max}} \mathbf{P}\left(\sqrt{\Delta^2 + l_z^2}\right) \Delta dl_z; \quad l_{z\max} = \sqrt{1 - \Delta^2}, \quad (\text{A15})$$

which after inserting from (A12) and integration with the use of [Mathematica](#) (2018) implies relation (18).

This work has made use of data from the European Space Agency (ESA) mission *Gaia* (<https://www.cosmos.esa.int/gaia>), processed by the *Gaia* Data Processing and Analysis Consortium (DPAC, <https://www.cosmos.esa.int/web/gaia/dpac/consortium>). Funding for the DPAC has been provided by national institutions, in particular the institutions participating in the *Gaia* Multilateral Agreement. The work was supported by the project LTT17018 of the MEYS (Czech Republic). Further, we are grateful to J.Grygar for deep interest and many valuable comments and J.Palouš and O.Teryaev for very useful discussions and inspiring comments.

REFERENCES

- | | |
|--|---|
| <p>Arenou, F., Luri, X., Babusiaux, C., et al. 2018, A&A, 616, A17</p> <p>Caballero, J. A. 2009, A&A, 507, 251</p> <p>Close, L. M., Richer, H. B., & Crabtree, D. R. 1990, AJ, 100, 1968</p> | <p><i>Gaia</i> Collaboration (Prusti T. et al.) 2016, A&A, 595, A1</p> <p><i>Gaia</i> Collaboration (Brown, A. G. A. et al.) 2016, A&A, 595, A2</p> <p><i>Gaia</i> Collaboration (Brown, A. G. A., et al.) 2018, A&A, 616, A1</p> |
|--|---|

Jiménez-Esteban, F. M., Solano, E. & Rodrigo, C. 2019, AJ, 157, 78
Wolfram Research, Inc., Mathematica, Version 11.3, Champaign, IL (2018)
Oelkers, R. J., Stassun, K. G., & Dhital, S. 2017, AJ, 153,259

Oh, S., Price-Whelan, A. M., Hogg, D. W., Morton, T. D., & Spergel, D. N. 2017, AJ, 153, 257
Zavada P. & Píška K., 2018, A&A, 614, A137
Ziegler C. et al. 2018, AJ, 156,259